Experimental and theoretical study of density, potential and current structures of a helium plasma in front of a RF antenna tilted with respect to the magnetic field lines

J. Ledig, E. Faudot, J. Moritz, S. Heuraux, N. Lemoine, S Devaux

Experimental and theoretical study of density, potential and current structures of a helium plasma in front of a RF antenna tilted with respect to the magnetic field lines

J. Ledig,[1, a)] E. Faudot,[1] J. Moritz,[1] S. Heuraux,[1] N. Lemoine,[1] and S. Devaux[1, 2]

[1)]*Université de Lorraine – Institut Jean Lamour, Campus Artem 2 allée André Guinier - BP 50840,*
54011 NANCY Cedex, France
[2)]*CRYOSCAN, Campus Artem 2 allée André Guinier - BP 50840, 54011 NANCY Cedex,*
France

Potential and density structures in the vicinity of a RF electrode/antenna in a magnetized plasma are investigated using a RF compensated cylindrical Langmuir probe. These measurements were performed in the ALINE plasma device in which only electrons can be considered as well magnetized. Very precise 2-D maps of the plasma parameters are drawn thanks to a 3-D automatic manipulator on which the probe is mounted. The effect of the tilted magnetic angle between the RF biased surface and the magnetic lines is also studied thanks to a tilting electrode. Comparison of several simplistic models with the experiments proved the reliability of simple Langmuir probe measurements in such a RF and magnetized environment (space potential v.s. tilting angle of the antenna with respect to magnetic field lines, and recovering of the floating potential structure using measured currents). A fluid model based on total current density, and ion diffusion equations over the biased flux tube, provides the same density structures in front of the electrode than the measurements. Those density structures display a "bunny ears" shape, and can be explained using transverse RF and collisional current behaviour: in front of the antenna the transverse ion currents deplete the magnetized flux tube, while at the edge of the biased flux tube, the same currents rise the density.

I. INTRODUCTION

Potential structures in a magnetized plasma have been investigated for a long time[1,2], in order to understand plama fluxes and to study the edge of Tokamak plasmas responsible for heat fluxes at the wall[3]. A DC or RF biased source is able to raise a strong potential structure in a magnetized plasma due to RF sheath rectification[4], and to induce convective cells all around the structure[5,6]. This phenomena are present in classical magnetized discharges (e.g. magnetron discharges) and in the scrape off layer (SOL) of tokamaks in which ICRH (Ion Cyclotron Resonant Heating) antennas[7] are able to generate such potential structures .

The comprehension of density and potential structures in front of these antennas/electrodes is really important to evaluate the heat fluxes responsible for hot spot on their surfaces, and to prevent the sputtering, heating and destruction of connected parts at the wall or on the RF antenna. In addition, the magnetic configuration is such that the surface of the RF antennae is not parallel nor perpendicular to magnetic field lines, but a little tilted[8] . Hence, the influence of the tilted angle of a biased electrode or antenna is treated here in the ALINE plasma device[9] in which the relative low RF power allows to make noiseless measurements.

To diagnose these potential structures, Langmuir probes can be used to get the plasma's main parameters, and probe measurements are technically speaking relatively easy to perform. There is already a large documentation on this subject[10–16] especially in a steady and non magnetized plasma where a Langmuir probe measurement can provide a robust estimation of the whole bulk plasma density, temperature and potentials (floating V_{fl} and plasma ϕ_p ones).

But the problem is more challenging when performing these measurements in a magnetized plasma[17–23] and even more when connected to a radio-frequency (RF) antenna/electrode[24–30]. Indeed, turning on the magnetic field breaks down isotropy and the probe measurement is then only defined locally (measured parameters can drastically change when moving across magnetic field lines). It is then needed to perform measurements into several areas of the plasma in order to access to the full structure of plasma parameters. But the most difficult issue is to understand how the current is collected by a cylindrical probe when it is aligned with magnetic field. This topic has been addressed by several authors in the case of strongly magnetized electrons[22,31]. But in the case of weakly magnetized ions, such as in small plasma discharges, the ion part in the $I(V)$ characteristics remains the best way to deduce the plasma density, particularly in RF environment because ions are less sensitive to RF oscillations[24]. On the electrons part of the characteristics, cylindrical probes exhibits a strong

---

a)Electronic mail: jordan.ledig@univ-lorraine.fr

slope break in the region of the plasma potential, so that it is much more convenient to locate ϕ_p than for a planar or spherical probes. In some cases, a bump rises on the $I(V)$ in this potential range, due to a density depletion of the biased plasma connected to the probe during a voltage ramp[21,32]. All of theses knowledge of numerous cylindrical probe theories have been reviewed to interpret probe data and to draw potential, density and temperature contour plots all around a RF electrode.

Two dimensional contour plots of plasma parameters have been measured experimentally in the 1 m long linear plasma device ALINE[9,32,33]. The antenna (also called electrode) was tilted with respect to the magnetic field lines. The measurements are faced to some models to check the reliability of the measurements in these specific conditions (RF + magnetic field). The protocol is described in section II. In Section III, the 2-D potentials and density maps are plotted and discussed. A first model predicting the spacial evolution of the plasma potential with respect to the inclination angle of the electrode is provided. A second one recovers the measured floating potential structure in front of the electrode as function of the measured density and plasma potential structures. Finally, section IV introduces a fluid model using the total current and ion flux conservation equations. The numerical solution of this model allows to recover the measured density profiles and to provide a physical explanation of the pumping phenomenon enhanced by transverse currents all along the RF biased plasma column.

II. EXPERIMENTAL DESIGN

A. Setup and protocol

All the measurements were carried out in the ALINE plasma device[9,33] (see scheme in Fig.3): a cylindrical vessel (1 m long and 30 cm diameter). Six coils are placed equidistantly along the chamber to generate a magnetic field up to 100 mT at the center of the cylinder (the input current goes up to 220 A). In the working volume, i.e. near the center of the vessel, magnetic field lines are along the z axis (i.e. the axis of the vessel) – as they would be in an infinite solenoid approximation – and the magnetic field amplitude can be supposed homogeneous, i.e. $\mathbf{B}(\mathbf{r}) = B_0 \mathbf{e}_z$. See ref.[32] for more informations on this device.

A circular RF antenna (8 cm diameter and 1 cm thick) is placed at the center of the vessel (see photograph in Fig.1). In the following work, the antenna is directly connected to the RF generator (without matching box). Ergo, the mean voltage on the antenna is 0 and the plasma potential is oscillating at the RF frequency ν_{RF}. The antenna can
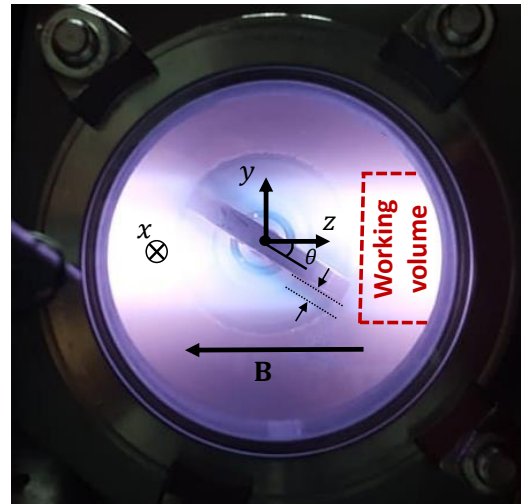

FIG. 1. Photograph of the electrode inclined with respect to the magnetic field/horizontal/z axis at 20 W, 94 mT and 3 Pa. The ~ 1 cm-thick sheath is distinguishable: less shiny plasma due to less electrons in it since they are repealed by the electrode. Note: sheaths appear around all biased surfaces with respect to the plasma, including the probe.

be tilted with respect to the magnetic field lines at any angle $\theta \in [0, 360]°$. Note that the antenna plays also the role of the electrode, and the rest of the vessel is the anode (thus $S_{\text{electrode}} \ll S_{\text{anode}}$). The input power can go from 20 up to 200 W, and the frequency range goes from 10 kHz up to 250 MHz. In the frame of this work, the RF frequency was set to 25 MHz.

The probe measurements obtained in this study are performed in a Helium plasma ($n \simeq 10^{16}$ m^{-3}). To get the plasma parameters, cylindrical Langmuir probe measurements were done inside the working volume, in front of the electrode. The choice of a cylindrical and thin probe (length $L_p = 1$ cm and radius $r_p = 75$ microns) was motivated because of a better spacial resolution: the measurement step in the y and z directions, Δy and Δz respectively., cannot be less than the probe dimensions (i.e. $\Delta y \geq r_p$ and $\Delta z \geq L_p$). To obtain a probe characteristic, a voltage ramp from -100 to 100 V at a frequency of 65 kHz was applied on the probe tip and the collected current is measured. The final $I(V)$ curve was the average over 20 successive voltage ramps. The probe tip is RF compensated to allow measurements in a radio-frequency discharge[24,34,35]. Since the voltage ramp rate is lower than ω_{RF} (78 Mrad/s), and both ω_{pi} (66 Mrad/s) and ω_{pe} (5.6 Grad/s), the measurement can be seen as stationary.

The Langmuir probe (also see ref.[32] for more informations) is held by a manipulator which allows us to perform measurements in a 3-D volume. The center of the electrode lays at the coordi-
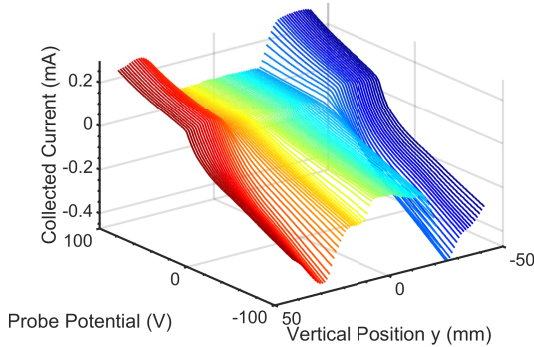
FIG. 2. The procedure applied for building the contour plot is the following: the probe is first fixed at a constant z position, and then moved in the y direction. Finally, the z position is changed. In this figure is depicted a y–profile of $I(V)$ characteristics at $z = 150$ mm, 94 mT, 3 Pa 25 MHz and 20 W, where the antenna is tilted by $\theta = 25°$.
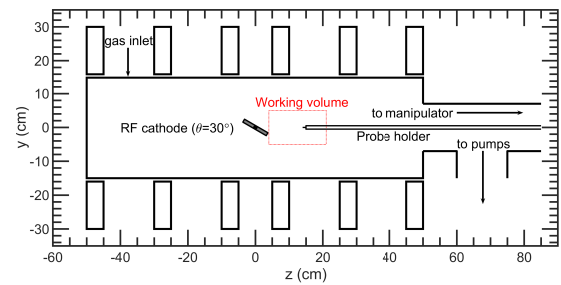

FIG. 3. The drawing of the ALINE plasma device (to scale, side view). Where the 12 rectangles on both sides of the chamber represent the coils. Magnetic field lines are parallel to the z direction, and its magnitude is constant in the working volume.

nates $(0,0,0)$. In the scope of this paper, the probing volume is the surface $\{x = 0, y \in [-42, 42], z \in [20, 200]\}$ mm with $\Delta y = 1$ mm and $\Delta z = 10$ mm (note that the z range is adjusted regarding the electrode inclination, and that the ion larmor radius is of the order of 400 μm at 94 mT). The y range is limited by the manipulator that can not go further away from its axis. A scan in the (x, y) is also performed with a thicker spatial resolution of $\Delta x = \Delta y = 2$ mm (around 1800 characteristics) in order to perform the measurement in a reasonable amount of time.

To obtain a 2-D contour plots of plasma parameters in front of the electrode, $I(V)$ curve measurements were performed at each node of the working volume grid and exploited using a simple and flexible – but reliable fitting method of the ion saturation current[36–38], and presented in section II C. Therefore one 2-D map needed over a thousand of Langmuir probe characteristics and several hours of acquisition (the ALINE plasma is stable enough to make this possible). A y–scan is depicted in Fig.2: one position z is associated to 82 characteristics. The gas pressure, the magnetic field amplitude, and the electrode inclination were changed during our experimental work to track their effects on the plasma parameters. However, the RF power is fixed at 20 W. The choice of low RF power is motivated by the fact that at hight power (*i*) the RF oscillations can lead to bad estimation of plasma parameters[24], (*ii*) the characteristic can display a bump between the exponential and the electron part[32] meaning that the measurement disturbs the plasma, and (*iii*) the long discharge time causes the electrode to heat up, changing the plasma conditions between the beginning and the end of the scan.

B. Dependency on potential and magnetic field

The effective collection surface of a Langmuir probe is dependant of the applied voltage on the probe tip, but also on the applied magnetic field. Indeed the existence of a magnetic field changes the motion of the particles: due to Lorentz force, they follow a cyclotron motion and turn around the magnetic field lines. The radius of charged particles around magnetic field lines – called Larmor radius – is smaller for electrons than for ions. Indeed, $\rho_c = v_\perp / \omega_c \approx \sqrt{k_B T_e m} / eB$ (where $\omega_c = eB/m$ is the cyclotron frequency, B the magnetic field amplitude, m the mass, and $k_B = 1.38$ J/K the Boltzmann constant). Therefore electrons are more confined than ions. This sensitivity to the magnetic field also changes the collection surface for each species[22,23]. In some cases the electron and ion current growth can even be similar in amplitude[39]. As it was shown in a previous paper, using a thin cylindrical probe in a magnetized plasma can lead to wrong estimation of the plasma parameters due to electron density depletion[18–21,39,40] once the applied voltage overcomes the plasma potential, $V > \phi_p$. Therefore, it is more convenient and reliable to work with the ion part of the $I(V)$ than with the electron part in magnetized conditions[41]. Anyway, the quasi-neutrality approximation allows us to state that ion density obtained with the ion part is close to the electron density, i.e. $n_i \approx n_e$ for single charged ions (which is the case in the ALINE experiments).

Since parallel to **B** transport is much higher than perpendicular transport, due to magnetic confinement, we can talk about "magnetic flux tubes". Indeed, perpendicular transport can be driven by collisions[42], biasing effects[43] or anomalous transport. In this work the "flux tubes" term references to the magnetic channel connected to the electrode on one end, and to the grounded wall on the other. Since the probe holder is made of ceramics, its po-

tential is floating and at low RF power, we assume that its presence does not disturb the flux tube.

Both, voltage and magnetic field dependency make it very difficult to extract plasma parameters from the $I(V)$. Finally, the RF fluctuations also distort the shape of the characteristics[24,27]. Indeed, having a RF power supply leads to oscillations of the plasma potential due to the auto-polarisation of plasma[29,30,44–48], moving the $I(V)$ "back and forth". And since the measurement is an average of this phenomenon, it leads to overestimation of the electron temperature (the exponential growth is wider). But the ion part remains more or less unchanged in the saturation region. This second argument explains our choice of using the ion part of the $I(V)$.

C. IV analysis

Theoretical processing of probe characteristics in magnetized plasmas is still an open research field. Lots of authors worked on this subject (Langmuir[15], Bohm[13], Laframboise[31,49], Chen[50], etc.[10,11,51–53]). A global overview on major theories is available herein[12]. Langmuir's Orbital Motion Limit (OML) model is simple to use and to apply because, assuming that there is no sheath, it states – under cold ions approximation – that $I_i^2(V)$ is a linear function, whose slope is proportional to the density squared and independent from the temperature. However our characteristics do not fit with this model (the RF has nothing to do with that though[25]). Using ABR[10,11] or BRL-Chen[52] theories would be a good option, but it is recommended to check if the output parameters and the fitting are correct for all characteristics ; nevertheless our cumbersome maps (containing over 1000 $I(V)$ each) do not allow us to do so. Laframboise[31,49] did a very deep work on the collection of charged particle by a cylindrical Langmuir probe in magnetized plasma. He computed the collected current, and his curves are universal because they only depend on the probe radius-to-electron Debye length ratio, r_p/λ_{De}. Unfortunately, there is no analytical expression available, but only numerical results. Chen did a parameterization of these curves, but the algorithm still needs a supervisor to check the fitting of the measured $I(V)$ because those method need some initial input parameters. Mausbach and Steinbrüchel[37,38] proposed to fit the ion current with the function $a(b + \chi)^c$, where a, b and c are fitting parameters and χ the normalized potential drop between the plasma and the probe, $e(\phi_p - V)/k_B T_e$. In our experiment we assume that the ion current is given by the relation[36],

$$I_i^{\text{theo}} = I_{i\text{sat}}(1 + \chi)^k, \tag{1}$$

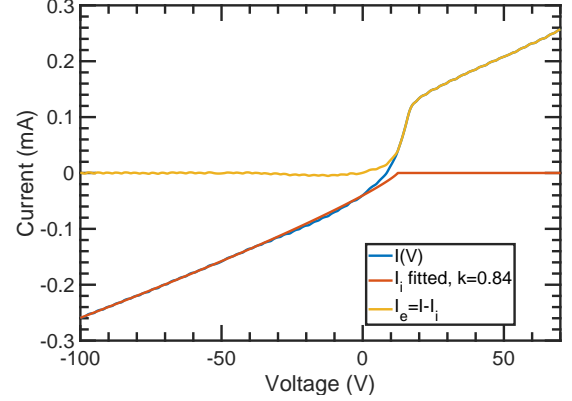

FIG. 4. Result of the numerical and automatic fitting of the ion current, allowing the determination of the plasma density $n = 3.7 \times 10^{15}$ m^{-3} and electron temperature $T_e = 4.9$ eV after two iterations.

with $I_{i\text{sat}} = -0.61 \times enc_s S_p$ (assuming $T_i \approx 0$ and thus $c_s = \sqrt{k_B T_e/M}$ with M the ion mass) the ion saturation current and $S_p = 2\pi r_p L_p$ the probe area. This parametrization allows us to ensure $I_i^{\text{theo}}(\phi_p) = I_{i\text{sat}}$.

The Algorithm

This algorithm was used to extract all parameters automatically, without input or guessed parameters, from the numerous characteristics measured: density n, plasma potential ϕ_p, probe floating potential V_{fl} and plasma temperature T_e.

a. Initialization: First of all, one needs to determine both plasma and floating potentials. The $I(V)$ is smoothed with a Savitzky-Golay algorithm[54] and the floating potential $V_{\text{fl}} = V(I = 0)$ is determined. The first derivative is computed numerically and smoothed again. The first maximum after the floating potential gives the position of the plasma potential ϕ_p, $\text{d}I/\text{d}V|_{\phi_p} = \max(\text{d}I/\text{d}V)$. Note: in the literature, the plasma potential is also called "space potential" in a magnetized plasma, because each magnetic flux tube can have its own potential. Nevertheless the RF distortions and the noisy second derivative makes the use of Druyvesteyn's theory[55] inapplicable (i.e. $\text{d}^2I/\text{d}V^2 \propto \text{EEDF}(V)$, the electron energy distribution function) even after another smoothing.

b. First fitting of I_i: Now, one needs to estimate the electron temperature. To do so, the ion current must be removed from the characteristic. In the range $V \in [-100, V_{\text{fl}} - 20]$ V, a linear fit[56] of the curve is performed: $I_i = C_1 V + C_2$.

c. First determination of T_e: Once I_i is known, it is possible to compute $I_e = I - I_i$. A linear

fit of $\ln I_e$ vs V is done in the range $V \in [V_{\text{fl}}, \phi_p]$ V, the slope being $e/k_B T_e$.

    d. Better fitting of I_i: With the last computed value of T_e, one can fit the ion current from the $I(V)$ in the same range as in *b.*, but this time using equation (1).

    e. Better determination of T_e: With this new fit of I_i, the electron current can be evaluated, and T_e can be determined the same way as presented in *c.*

    f. Loop and convergence: The new value of T_e is compared to the old one, and if $|T_e^{\text{new}} - T_e^{\text{old}}| > \varepsilon$, the algorithm starts again at point *d.* The convergence is achieved within less than 5 loops generally ($\varepsilon = 0.2$ eV is chosen). The last value of $I_{i\text{sat}}$ obtained in the loop is used to estimate the density:

$$n_{\text{fit}} = -\frac{I_{i\text{sat}}}{0.61 \times e S_p \sqrt{k_B T_e^{\text{new}}/M}}, \qquad (2)$$

The result of a fit is depicted in Fig.4. The discontinuity is due to the fact that the model do not take into account the region above plasma potential. We assume that, if this method do not give the precise estimate of n and T_e it can provide, at least, their spatial evolution.

III. TWO-DIMENSIONAL CONTOUR PLOTS OF PLASMA PARAMETERS

    The data will be presented on 2-D heat maps, so that every map represents the spacial structure of a given quantity, $Q(x = 0, y, z)$. All measurements were obtained in a single plane in front of the electrode in one discharge (i.e. it is the same plasma from the first point until the last one). The dashed lines on the following graphs delimits the "top" of the electrode (which also coincides with the top of the bright plasma, see Fig.1). For safety reasons, measurements are done with spatial margins (avoiding the probe to hit the electrode), thus inducing different probing areas in the z direction ($\parallel B$).

    Since heat maps plots are cumbersome, it is not possible, in the scope of this paper, to show all of them. We have chosen to depict the spatial evolution of the plasma parameters with respect to the inclination of the antenna/electrode for only one discharge condition: 20 W input RF-power, 3 Pa He pressure and 94 mT magnetic field. This gives six plots for each parameter and provides a good overview on the structure evolution with respect to the tilting angle. To compare with what happens at low field or at low pressure, two more plots are added at the inclination of $45°$ (one at 1.5 Pa, the other at 47 mT) and still with 20 W RF-input power.

    This section will mainly yield a qualitative overview of several plasma parameters evolution with respect to the position, the magnetic field amplitude, the pressure and the inclination of the electrode. An attempt of understanding quantitatively the experimental outputs will be done in the next section.

    However, the plasma temperature will not be presented in this study because of the big uncertainty in its determination: magnetic field and RF fields makes it very difficult to get reliable values due to the distortion of the characteristics in the exponential part. Nevertheless, measurements showed that the electron temperature is rather constant inside the flux tube, few centimetres away from the electrode. Therefore, T_e is assumed to be equal to 5 eV and constant in the rest of the paper.

A. Plasma potential

    This subsection refers to figures 5(a) to 5(h). It is clear that the plasma channel in front of the electrode is biased with respect to the the "bulk" plasma (ouside the channel). In addition, the bigger the section of the flux tube, the higher is the biasing[29]: at $0°$ (Fig.5(a)) the channel diameter is $d_c = 1$ cm and the potential difference between inside and outside the magnetic channel is $\Delta \phi_p = \phi_p^{\text{in}} - \phi_p^{\text{out}} \approx 5$ V, whereas at $90°$ (Fig.5(f)) the channel diameter $d_c = 8$ cm and $\Delta \phi_p = \phi_p^{\text{in}} - \phi_p^{\text{out}} \approx 25$ V.

    For lower magnetic field (Fig.5(g)), the plasma is less confined, and thus, the perpendicular transport is higher: the plasma potential structure is shorter than with a 94 mT magnetic field amplitude. In the opposite, at low pressure (Fig.5(h)), the structure is longer, because there are less collisions, and each flux tube remains disconnected from each other.

    Moreover, these maps reveal the existence of a transverse electric field, $E_y = -\partial_y \phi_p$, at the edge of the magnetic flux tube. This electric field also generates a drift of charged particles in the x-direction due to the $\mathbf{E} \times \mathbf{B}$ drift: $u_x = E_y/B$ (see Fig.6). The drift velocity in the Hall direction approaches 10 km/s at the edge of the potential structure.

    According to the measurements, the plasma potential displays a plateau in the middle of the structure in the z direction. We were able to measure the evolution of this plateau amplitude with respect to the tilting angle θ. This measurement was achieved at 3 Pa, for $B_0 = 94$ mT and for several input RF power (from 13 to 79 W) at the location $x = 0$ mm, $y = 0$ mm and averaged over the range of $80 \leq z \leq 110$ mm. The plot of $\phi_p(\theta)$ are alike for all powers: similar shape, but an up-shift with increasing power. Therefore, all plasma potential vs. θ is normalized to their value at $\theta = 90°$ (light coloured curves in Fig.7) and the averaged curved was computed (red curve with errorbars). All curves superimpose very well.

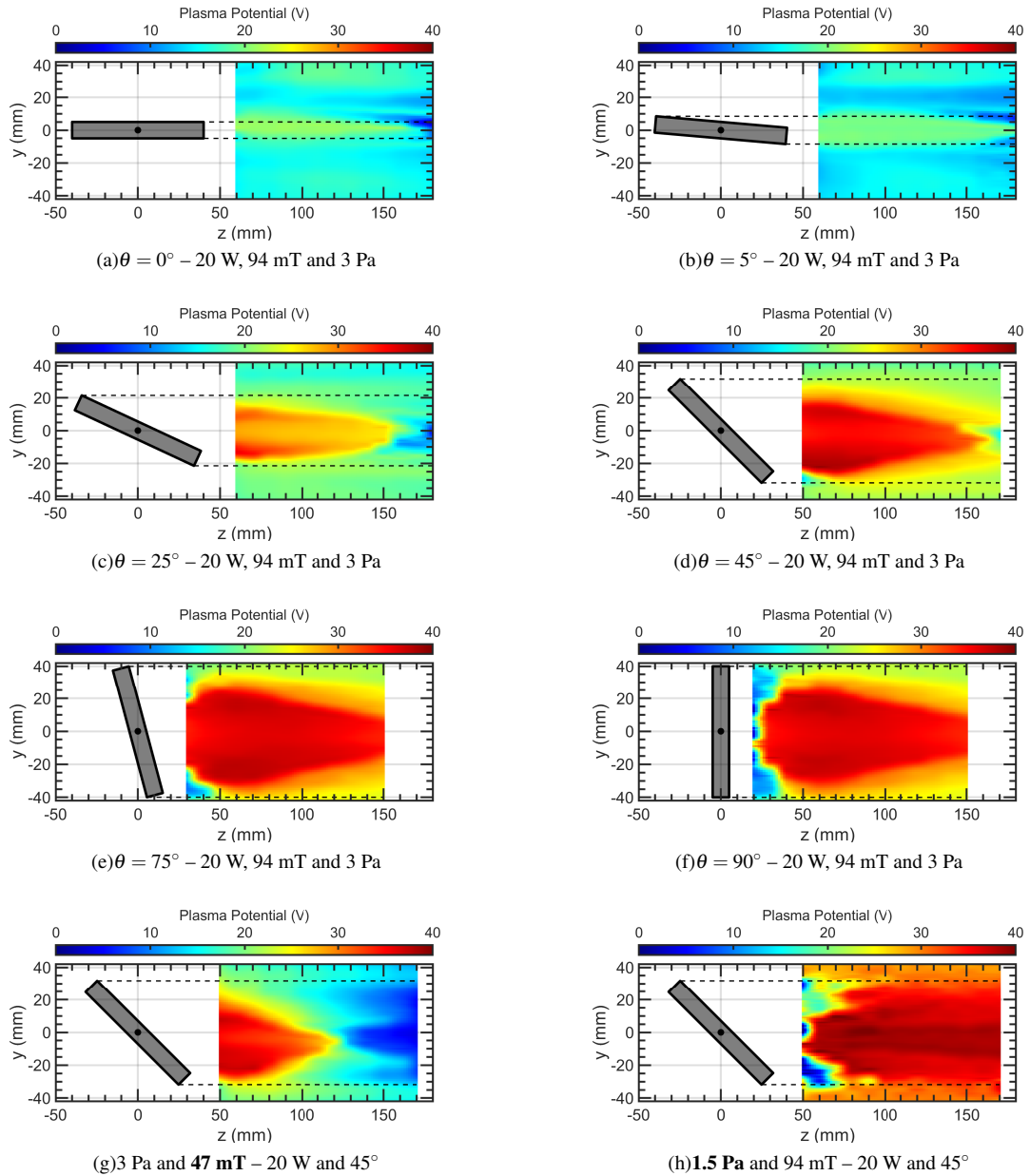FIG. 5. Plasma potential contour plots in front of the RF antenna, for $\nu_{RF} = 25$ MHz. Conditions are labelled below each plot. For (a) to (f): 1 discharge, all inclination. For (h) & (g) comparisons at 45° for low field and low pressure condition respectively Note that the potential axis do not have the same range as the V_{fl} plots. (a) $\theta = 0°$ – 20 W, 94 mT and 3 Pa, (b) $\theta = 5°$ – 20 W, 94 mT and 3 Pa, (c) $\theta = 25°$ – 20 W, 94 mT and 3 Pa, (d) $\theta = 45°$ – 20 W, 94 mT and 3 Pa, (e) $\theta = 75°$ – 20 W, 94 mT and 3 Pa, (f) $\theta = 90°$ – 20 W, 94 mT and 3 Pa, (g) $\theta = 45°$ – 20 W, 47 mT and 3 Pa and (h) $\theta = 45°$ – 20 W, 94 mT and 1.5 Pa.
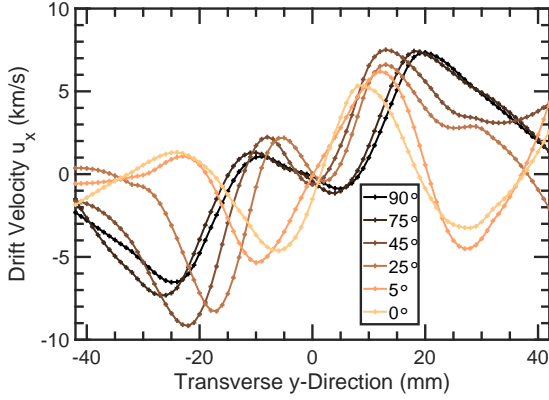
FIG. 6. Spatial evolution of the drift velocity $u_x = \partial_y \phi_p / B$ at 94 mT, 3 Pa, obtained by taking $\phi_p(y, z = 100\,\text{mm})$ from the 2-D maps, in the direction $\perp \mathbf{B}$.
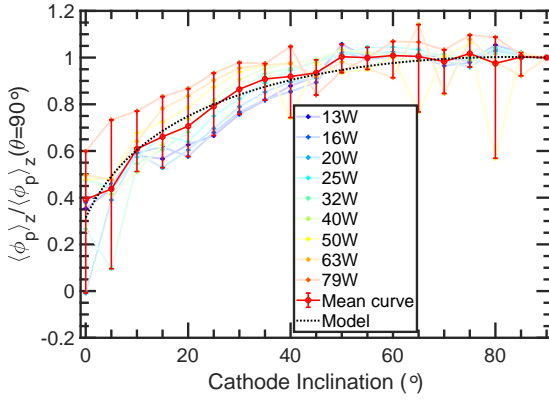

FIG. 7. Evolution of the plateau amplitude of the plasma potential structure with respect to the inclination of the electrode with respect to the magnetic field lines.

A simple flux tube model was built to understand this averaged curve. First of all, we assume that the section of the flux tube in front of the electrode is a thick disk of diameter d_c, and depends on the inclination of the probe:

$$d_c \approx 2R_c \sin\theta + T_c \cos\theta \quad (3)$$

where $R_c = 4$ cm and $T_c = 1$ cm are the electrode radius and thickness respectively. The frontal surface of the tube is then $S_F = \pi d_c^2/4$, and the lateral surface is $S_L = \pi d_c L_{\parallel}$ ($L_{\parallel}$ is the length of the magnetic flux tube, i.e. the distance electrode – grounded wall). We then assume perfectly confined electrons, and unmagnetized ions. The discharge model seen in the point of view of electrons and ions are given in figures 8(a) and 8(b) respectively. Next, one assumes the current density conservation all over the flux tube boundaries. Recall that $J_{e,\text{sat}} = 0.25en\langle v_e\rangle$ the electron saturation current density in the approximation of Maxwellian elec-

trons ($\langle v_e\rangle = (8k_B T_e/\pi m)^{1/2}$), and $J_{i,\text{sat}} = 0.61enc_s$ the cold ion saturation current density. Current density conservation of the magnetic flux tube, considering collisionless sheath and the absence of secondary electrons, writes:

$$0 = \sum_{k=i,e} J_k \times S_k$$
$$\Leftrightarrow 0 = J_{i,\text{sat}}(2S_F + S_L)$$
$$\quad - J_{e,\text{sat}} S_F \left(e^{\varphi_{\text{RF}} - \varphi_p} + e^{-\varphi_p}\right) \quad (4)$$

were φ are normalized potentials to $e/k_B T_e$. Let us now define the plasma floating potential (different from the probe one) to lighten the equations as the ratio :

$$\varphi_{\text{fl}} \equiv \ln\left(\frac{J_{e,\text{sat}}}{J_{i,\text{sat}}}\right) \approx 4.02. \quad (5)$$

Equation (4) gives the expression of the plasma-or-space potential in the magnetic flux tube,

$$\varphi_p = \varphi_{\text{fl}} + \ln\left(1 + e^{\varphi_{\text{RF}}}\right) - \ln\left(1 + 2\frac{L_{\parallel}}{d_c}\right) - \ln 2 \quad (6)$$

Averaging it over time, the second term can be approximated[4,47] by $\tilde{\varphi}_{\text{RF}}/\pi$. Therefore, the measured plasma potential can be approached by the equation:

$$\langle\varphi_p\rangle_t = \varphi_0 - \ln\left(1 + \frac{2L_{\parallel}}{2R_c \sin\theta + T_c \cos\theta}\right) \quad (7)$$

for $\varphi_0 \sim \varphi_{\text{fl}} - \ln 2 + \tilde{\varphi}_{\text{RF}}/\pi$. This equation is also plotted in Fig.7 in black dashed line. Since experiment and model are in good agreement, the hypothesis of unmagnetized ions is verified, i.e. ions undergo to one or more collisions during a cyclotron period ($\nu_{iN} > \omega_{ci}$). In addition to that, if ions were magnetised, the third term in Eq.(6) would vanish together with the angle dependence and the model would not be able to reproduce the trend of the measurements. Moreover, this suggests that the measurements done in magnetized and RF conditions seem reliable and exploitable, which is encouraging. This result also highlights the fact that for a parallel antenna, the "active" surface is rather small, and thus, the self-biasing of the facing plasma is also small. On the opposite, as the antenna is tilted, the "active" surface of the antenna increases and thus the self bias becomes significant[29].

Finally, the spacial shape of the plasma potential structure appearing in figures 5(a) to 5(h), i.e. $\phi_p(y)$, has a more complicated structure to understand and is coupled with the density structure. That is why the next section is devoted to this study, using a fluid model.
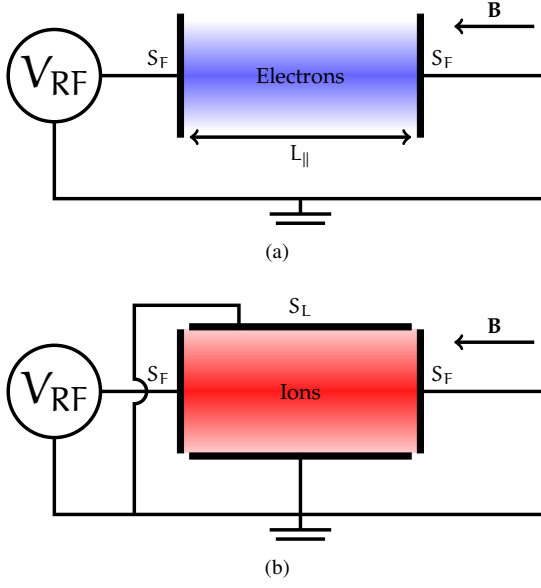
FIG. 8. Sketch of the used model. (a) Electron collection area and (b) Ion collection area.

B. Plasma density

This subsection refers to figures 9(a) to 9(h). The spatial structure of the plasma density shows a plasma density depletion in the magnetic flux tube connected to the electrode. This was already visible on the raw $I(V)$ in Fig.2 where the collected current is lower inside than outside the electrode flux tube. This is due in part by transverse RF currents[57] and by DC transverse currents[43]. The biased flux tube being positive compared to the surrounding plasma potential, ion current tend to leave the biased structure, while electrons are longitudinally expelled from the flux tube to maintain the quasi-neutrality. This mechanism explains the central plasma depletion and why the border of the biased channel is highlighted by a peak of density. The next section will provide a model to understand this observation properly.

Density structures also generate currents, called diffusion currents density $\mathbf{J}_\perp \propto -qnD_\perp \nabla_\perp n$, which in turn leads to electron drift around magnetic field lines (ions do not drift because they are un-magnetized). This is commonly known as the electron diamagnetic current density[6],

$$\mathbf{J}_{\mathrm{D}e} = \frac{\mathbf{B} \times \nabla p}{B^2} \qquad (8)$$

where $p = nk_BT_e$ the electron pressure in the approximation of a perfect gas.

At low magnetic field, Fig.9(g), the lower confinement allows to fill in the depleted channel at higher rate. That is, there is almost no clear difference between the inside and the outside in terms

of density number except at the edge of the biased flux tube, where transverse ion currents occur.

Finally, at low pressure, collisions are less important and the confinement is enhanced. This is perfectly demonstrated by the mesh plot in Fig.9(h): the inside of the channel depicts a density plateau at 5×10^{15} m^{-3} whereas the bulk plasma rather be at 12×10^{15} m^{-3} and the transition is done abruptly within 5 mm across magnetic field lines. In this regime the transverse currents are the most important.

C. Floating potential

This subsection refers to the plots 10(a) and 10(b). Unfortunately, the floating potential is the consequence of current balance on the probe ($I_e = |I_i|$) and depends implicitly on the collection surfaces, but since electrons and ions do not reach the probe in the same way (effective collection surfaces are different[22,23,32]) it is more complicated to evaluate on which part of the probe the collection is done. Moreover, the floating potential depends more on transverse electron fluxes than others: un-magnetized ion flux collected by all the probe area are low due to low ion velocity and the longitudinal electron flux magnetically connected to the probe is only collected on the front area of the probe depending on the probe radius and electron Larmor radius which are very small as well ($\pi r_p^2 \ll 2\pi L_p r_p$).

Outside the channel the floating potential stays homogeneous, while inside, near the electrode, the floating potential increases, and then decreases with z.

Nevertheless, since floating potential is a result of all other plasma parameters, because it describes $|I_e| = I_i$ at the probe: it depends on n, T_e and ϕ_p and especially on perpendicular fluxes, as explained above. Hence, it is more consistent to work in a (x,y) plane, perpendicular to magnetic field lines. The purpose of that kind of plot is to track the transverse currents.

To access to the transverse currents densities ($\perp$ $\mathbf{B}$), a 2-D scan is then performed in the (x,y) plane at 20 W, 1.5 Pa and 94 mT (with these conditions the magnetic channel is almost perfectly confined – as discussed in previous subsections). This scan is a result of over 1800 $I(V)$, in front of the electrode, at $z = 15$ cm (far enough from the electrode so that it does not perturb the V_{fl} value). The same routine is adopted to compute all plasma parameters, but only the floating potential is plotted in Fig.11(b).

According to equation (8), knowing plasma density and average temperature (~ 5 eV), one is able to compute the electron diamagnetic current density
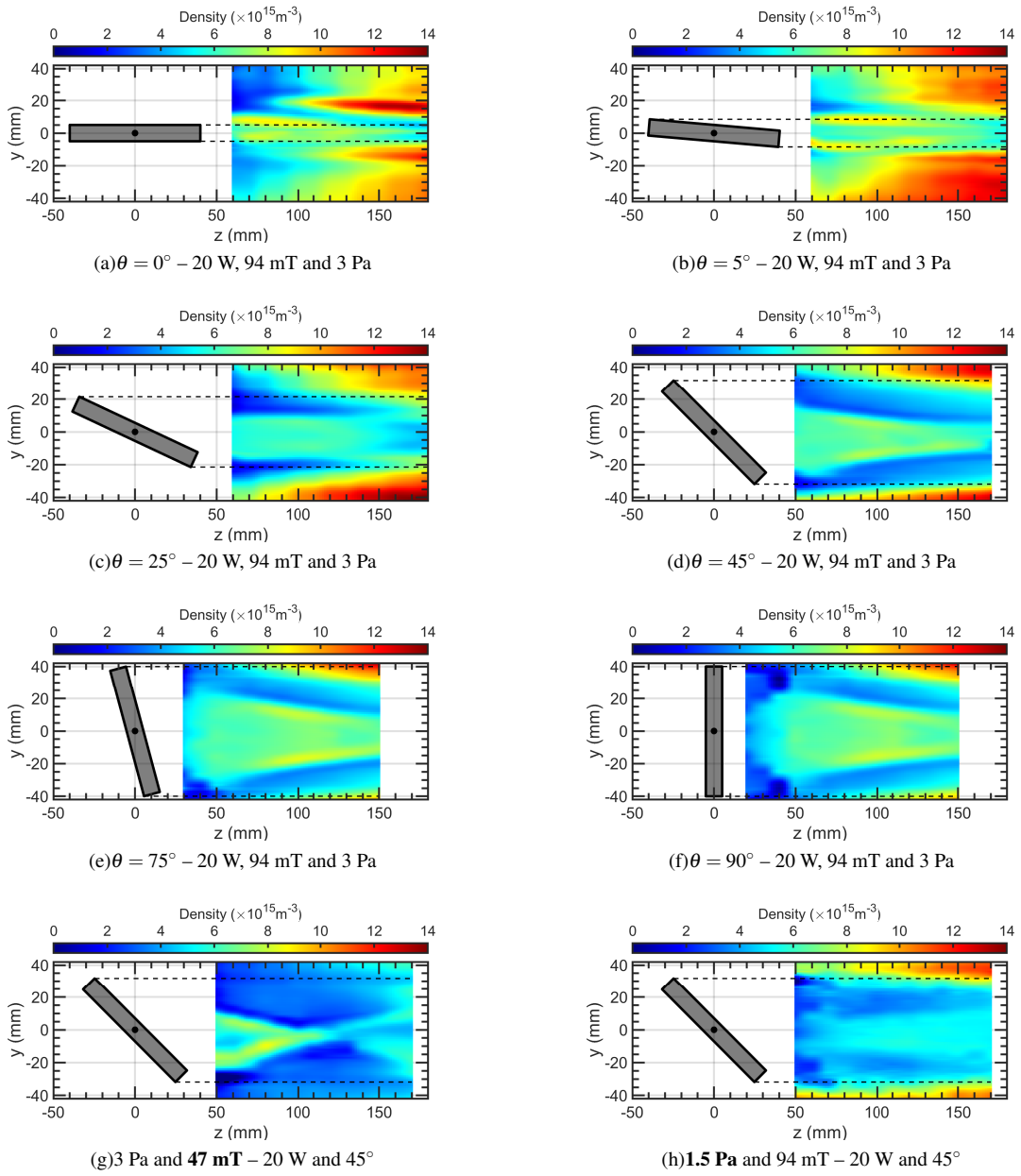
FIG. 9. Plasma density contour plots in front of the RF antenna, for $\nu_{RF} = 25$ MHz. Conditions are labelled below each plot. For (a) to (f): 1 discharge, all inclination. For (h) & (g) comparisons at 45° for low field and low pressure condition respectively. (a) $\theta = 0° - 20$ W, 94 mT and 3 Pa, (b) $\theta = 5° - 20$ W, 94 mT and 3 Pa, (c) $\theta = 25° - 20$ W, 94 mT and 3 Pa, (d) $\theta = 45° - 20$ W, 94 mT and 3 Pa, (e) $\theta = 75° - 20$ W, 94 mT and 3 Pa, (f) $\theta = 90° - 20$ W, 94 mT and 3 Pa, (g) $\theta = 45° - 20$ W, 47 mT and 3 Pa and (h) $\theta = 45° - 20$ W, 94 mT and 1.5 Pa.

(a)$\theta = 0° - 20$ W, 94 mT and 3 Pa

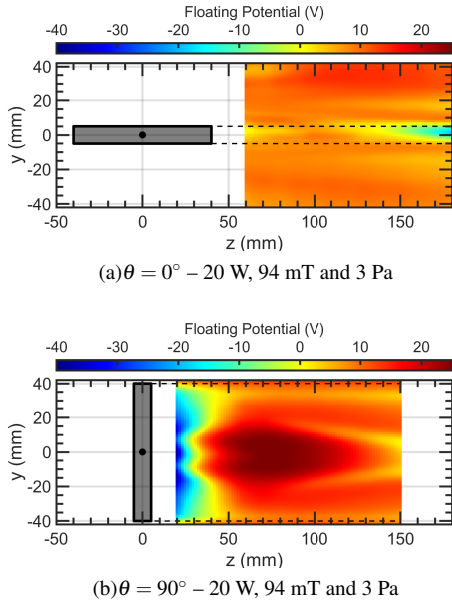(b)$\theta = 90° - 20$ W, 94 mT and 3 Pa

FIG. 10. Floating potential contour plots in front of the RF antenna, for $\nu_{RF} = 25$ MHz, of aligned and normal electrode with magnetic field lines. (a) $\theta = 0° - 20$ W, 94 mT and 3 Pa, (b) $\theta = 90° - 20$ W, 94 mT and 3 Pa.

field,

$$\mathbf{J}_{\mathrm{D}e} = \frac{k_B T_e}{B} \mathbf{e}_z \times \boldsymbol{\nabla} n, \tag{9}$$

but also the drift current density,

$$\mathbf{J}_{\mathrm{D}} = en\frac{\mathbf{e}_z}{B} \times \boldsymbol{\nabla} \phi_p. \tag{10}$$

The sum of all transverse current density field, $\mathbf{J}_\perp = \mathbf{J}_{\mathrm{D}} + \mathbf{J}_{\mathrm{D}e}$, is plotted on the measured floating potential map (arrows on Fig.11(b)). The amplitude of the diamagnetic drift velocity, $u_{\mathrm{D}e} = J_{\mathrm{D}e}/en$ is within the range of 10 to 50 km/s (for recall, $u_{e\parallel} \simeq \langle v_e \rangle \sim 10^6$ m/s is still much larger). One can see that the stream lines follows the V_{fl} structure, and that electrons streams around the antenna's channel anticlockwise. One can also notice that the electron transverse flux drifts around the magnetic channel connected to the antenna, and that there is no net perpendicular flux contributing to a depleting or re-fueling of the core plasma connected to the antenna. The assumption $\mathbf{J}_e = \mathbf{J}_{e\parallel}$ is verified.

Finally, in order to compute the probe floating potential using only measured quantities, we assume unmagnetized cold ions which are collected by the whole probe and magnetized and maxwellian electrons which are collected by only a small fraction of the probe, that we assume to represent approximatively 10% of the probe[22,23], which is actually the effective probe collecting area for the parallel flux at such magnetic field magnitudes (50-100 mT). In addition to those magnetized electrons

(a)Measured floating potential of the probe.

(b)Measured floating potential of the probe.
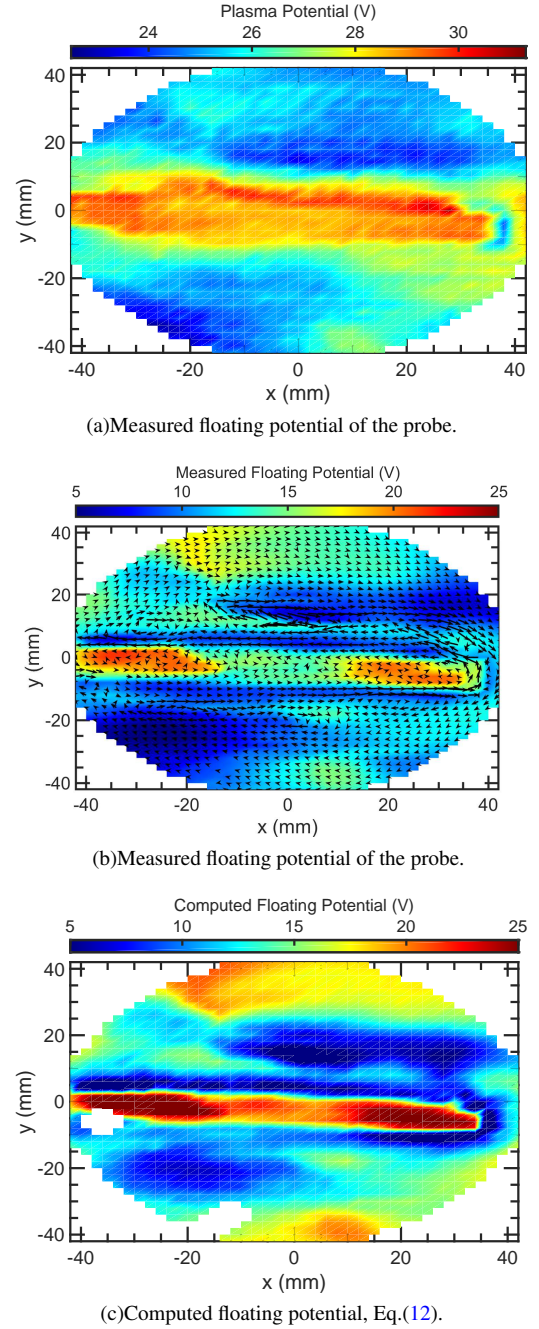

(c)Computed floating potential, Eq.(12).

FIG. 11. Plasma and floating potential contour plots in front of the RF antenna. The electrode has its center at $(0,0)$ and is 1 cm thick and 8 cm diameter, with tilt angle equal to $0°$. The magnetic field points towards the reader. Conditions: 1.5 Pa, 94 mT, $0°$, $z = 15$ cm.(a) Measured plasma potential, (b) Measured floating potential of the probe. The electron transverse current density field is plotted, (c) Reconstruction of the probe floating potential according to our model in Eq.(12). White regions are location where imaginary numbers were returned by the calculation.

we must add the transverse electron current density which we assume to be collected by only a portion κ of the probe. Therefore, floating condition implies:

$$J_{i,\text{sat}} S_p = \left(\frac{J_{e,\text{sat}}}{10} e^{e(V_{\text{fl}} - \phi_p)/k_B T_e} + \kappa J_\perp \right) S_p, \quad (11)$$

leading to the modified floating potential formula,

$$V_{\text{fl}} = \phi_p - \frac{k_B T_e}{e} \ln \left(\frac{J_{e,\text{sat}}}{10 J_{i,\text{sat}}} \right) + \frac{k_B T_e}{e} \ln \left(1 - \frac{\kappa J_\perp}{J_{i,\text{sat}}} \right). \quad (12)$$

The result is plotted in figure 11(c), where we have taken $\kappa = 0.25$. For a directed flux, κ should have been equal to 0.5 (the flux reaches the probe following only one direction). However, 0.25 gives a better fitting on the experimental curves, and can be due to the fact that the measured currents are not perfectly perpendicular: there is a parallel component which is not taken into account in the model (since the frontal surface is smaller than the lateral one).

The computed floating potential matches pretty well with the measured data. The comparison of the floating potential map with the plasma potential one, Fig.11(a), shows that $V_{\text{fl}}(x,y)$ is not only a shifted value of $\phi_p(x,y)$ (as suggested by the "classical" probe theory, $\phi_p - V_{\text{fl}} \propto T_e$). This observation seems to indicate that (*i*) transverse currents do exist (*ii*) transverse currents drive the evolution of the measured probe floating potential (*iii*) the measurements done using a cylindrical Langmuir probe are reliable.

D. Summary of the observations

In this section we have qualitatively described the evolution of the several plasma parameters in front of a tilted electrode in magnetized conditions by the mean of numerous cylindrical Langmuir probe measurements. The measurements evidenced the existence of a magnetic flux tube connected to the electrode, and following magnetic field lines. This channel is different from the bulk plasma, because its potential and temperature are higher, whereas its density is lower. The larger potential is explained by self biasing of the plasma in front of a RF biased surface. And the density depletion is due to perpendicular currents that pushes out ions from the channel[29,43], which is enhanced by RF transverse currents[58]. Along with this, the magnetic confinement is visibly improved when increasing the magnetic field, and when decreasing the pressure (leading to less collisions and less perpendicular diffusion). However, 1.5 Pa would be a good compromise to develop a fluid model based on the flux tube approximation because electrons and ions can both be seen as magnetized at low pressure.

The measurement allowed us to understand a bit more the behaviour of a biased and magnetized plasma channel in ALINE. First, a simple model was developed to prove that ions are not magnetized (using $\phi_p(\theta)$, Fig.7 and Eq.(6)). In addition, it was shown, by making a scan on a plane normal to the magnetic field lines, that electron diamagnetic currents are important in the building of the structures in front of the electrode (figure 11(c)).

However, the physical models in this section are quite simple, and not able to explain the particular shape of the plasma potential and density structures. That is why a more complex model is required, as depicted in the next section.

IV. FLUID MODEL

This quasy-neutral slab model is able to compute the potential and the density profile in front of the antenna, $\phi(t,y)$ and $n(y)$, using the total current density continuity and the ion flux conservation[27,28,57] with sheath boundary conditions. However, due the non-linearity of the equations it is not possible to provide an analytical solution, therefore the resolution will be implemented numerically. The following model solve the evolution of density n and the space potential ϕ in the y (or $\perp$) direction.

First, we are going to solve the space potential profile in front of the electrode using the total current density conservation:

$$\boldsymbol{\nabla} \cdot \mathbf{J}_{\text{Tot}} = \boldsymbol{\nabla} \cdot (\mathbf{J}_e + \mathbf{J}_i) = 0 \quad (13)$$

The space potential solution of this equation will be used to solve the density profile using the conservation of the steady state ion flux,

$$\boldsymbol{\nabla} \cdot (n\mathbf{u}_i) = S \quad (14)$$

with S the ion source term. Solving both equations at once is in general numerically unstable (because of an explicit scheme), therefore (13) is solved using a constant density profile as a guess: we therefore use an iterative method: inserting the obtained density profile from Eq.(14) into Eq.(13) again, and the newly obtained density profile is unchanged from the prior one, therefore one iteration is enough. The current density conservation, Eq.(13), depends both on space and time in order to solve the RF fluctuations. Its solution is then averaged over an RF period to be injected in the second equation, Eq.(14), which is steady state.

We are assuming a magnetic flux tube with perfectly magnetized electrons (i.e. $\mathbf{J}_{e\perp} = \mathbf{0}$), using

the same approach as described in Fig.8(a) and Fig.8(b). The channel is connected on the one side to the RF antenna, and on the other side to the grounded wall. The ions are weakly magnetized, and can move across magnetic field lines. The ions perpendicular current density is given by:

$$\mathbf{J}_{i\perp} = \mathbf{J}_{\text{pol}} + \mathbf{J}_{\text{mob}} + \mathbf{J}_{\text{diff}}$$
$$= \frac{Mn}{B^2}\frac{\partial \mathbf{E}}{\partial t} + en\mu_{i\perp}\mathbf{E} - eD_{i\perp}\boldsymbol{\nabla}n \qquad (15)$$

681 which are respectively the currents densities of,
682 polarization[27], mobility and diffusion[59]. M is the
683 ion mass, $\mu_{i\perp}$ is the ion transverse mobility coeffi-
684 cient, and $D_{i\perp}$ is the ion transverse diffusion coeffi-
685 cient.

686 **A.   Solving the potential profile**

First, we focus on solving the equation (13) to find a solution for the space potential ϕ in front of the electrode. As we assume constant density in this first step of calculation, the ion diffusion cur-rent density is neglected. Integrating (13) along the magnetic flux tube of length $L_\parallel$, and assuming ho-mogeneous currents densities along the flux tube, leads to:

$$0 = \int_0^{L_\parallel} \boldsymbol{\nabla}\cdot\mathbf{J}_{\text{Tot}}\mathrm{d}z = \int_0^{L_\parallel} \frac{\partial J_\parallel}{\partial z} + \boldsymbol{\nabla}_\perp\cdot\mathbf{J}_{i\perp}\,\mathrm{d}z$$
$$= 2J_{i,\text{sat}} - J_{e,\text{sat}}\left(1 + e^{\varphi_{\text{RF}}}\right)e^{-\varphi} + L_\parallel\boldsymbol{\nabla}_\perp\cdot\mathbf{J}_{i\perp} \qquad (16)$$

687 where potentials are normalized to e/k_BT_e. The par-
688 allel current density is only defined by the sheath
689 boundary conditions, assuming the parallel electric
690 field is equal to zero into the neutral plasma (no pre-
691 sheath in this model[47]). Injecting now expression
692 (15) into Eq.(16), one will get

$$1 - \frac{e^{\varphi_{\text{fl}}-\varphi}}{2}\left(1 + e^{\varphi_{\text{RF}}}\right) = C_\perp\eta\rho_{ci}\frac{\partial\Delta\varphi}{\partial t} + \beta\Lambda^2\Delta_\perp\varphi \qquad (17)$$

693 where $C_\perp = \varepsilon_0 L_\parallel\omega_{pi}^2/\omega_{ci}^2$ is the perpendicular ca-
694 pacitance of the flux tube[27], $\eta = M\omega_{ci}/(2\times$
695 $0.61ne^2)$ is the resistivity (which depends on n) and
696 $\Lambda^2 = L_\parallel D_{i\perp}/(2\times 0.61c_s)$ is the typical squared dif-
697 fusion length. A modified Einstein's relation is used
698 here, $\mu \equiv \beta|q|D/k_BT_e$ to add a last degree of free-
699 dom to the system ($\beta = 1$ do not provide a good
700 final result). In this equation we can see that the RF
701 leads to a capacitive behaviour of the flux tube.
702   To be able to solve the problem, we assume a
703 known profile shape for the RF potential $\varphi_{\text{RF}}(y,t) =$
704 $\tilde{\varphi}_{\text{RF}}f(y)\sin(\omega t)$. A Gaussian profile of amplitude
705 $\tilde{\varphi}_{\text{RF}}$ is not adequate regarding to the potential struc-
706 tures obtained experimentally (plotted in figures
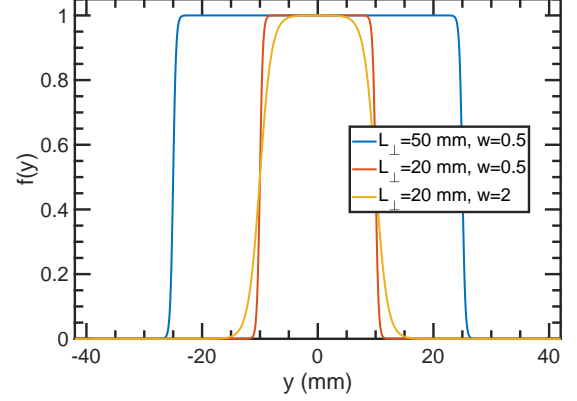707 5(a) to 5(h)) which depict a plateau in front of the

FIG. 12. Ad hoc spatial structure used for the initial RF potential.

708 antenna. The following profile is therefore chosen,
709 being a compromise between a Gaussian and a gate
710 function (avoiding discontinuities on the edge of a
711 pure square shaped function):

$$f(y) = \frac{\tanh\left(\dfrac{y+L_\perp/2}{w}\right) - \tanh\left(\dfrac{y-L_\perp/2}{w}\right)}{2\tanh(L_\perp/2w)} \qquad (18)$$

712 where $L_\perp$ is the diameter of the flux tube, and w
713 the typical potential gradient width of our structure
714 at $t = 0$: when $w \to 0$, f turns into a gate func-
715 tion, whereas f turns into a Gaussian as w increases.
716 Some examples are plotted in Fig.12. Now, equa-
717 tion (17) can be solved numerically using finite el-
718 ement methods (see appendix A). The resolution
719 provides the time evolution potential profile in front
720 of the cathode, $\varphi(y,t)$.

721 **B.   Solving the steady state density profile**

722   Now that we know $\varphi(y,t)$ it is possible to com-
723 pute $n(y)$. However, to simplify the problem, we do
724 consider the steady state of the density profile (i.e.
725 $\partial_t n = 0$). We define the RF currents densities as,

$$J_{\text{RF}} = -\frac{L_\parallel}{T_{\text{RF}}}\int_0^{T_{\text{RF}}}\boldsymbol{\nabla}_\perp\cdot\mathbf{J}_{i\perp}\,\mathrm{d}t \qquad (19)$$

726 from equation (16), averaged over one RF period.
727 Therefore, inserting this into the ion flux conserva-
728 tion equation (14) but this time taking into account
729 the diffusion flux, one will get

$$S = \frac{\partial\Gamma_{i\parallel}}{\partial z} - \frac{J_{\text{RF}}}{eL_\parallel} - D_{i\perp}\Delta n \qquad (20)$$

730 After integration along the flux tube of length $L_\parallel$,
731 the first term of the r.h.s. is a loss term equal to

the outwards ion flux, $2\alpha n c_s$, while l.h.s., S, is the source term playing the role of a constant ionization rate in order to maintain the density. Then, $SL_\parallel$ can be written as a constant saturation current density, $2\alpha n_0 c_s$. Finally $n(y)$ can be computed from following equation by matrix method: (see appendix B):

$$\Delta_\perp n - \frac{n}{\Lambda^2} = -\frac{J_{\mathrm{RF}}}{eD_{i\perp}L_\parallel} - \frac{n_0}{\Lambda^2}. \qquad (21)$$

with Λ^2 still equals to $L_\parallel D_{i\perp}/2\alpha c_s$, the typical diffusion length squared.

C. Code results and discussions

The free parameters in our model are temperature (which is assumed constant) T_e, "bulk density" n_0, transverse diffusion $D_{i\perp}$, transverse mobility $\mu_{i\perp}$ through the β coefficient, the parallel scale $L_\parallel$, the perpendicular scale $L_\perp$ (linked to θ), the RF amplitude V_{RF} and the wheelbase w (i.e. the size of the transverse gradients). Those seven parameters are adjusted by error/test method to get a density structure close to the experimental measurements. However, there are numerous ways to fit the measurements due to the seven degrees of freedom offered by our model. Therefore, the exploitation of the code output can only be done qualitatively.

The code is used to fit the experimental density profiles $n(y)$ at $z = 15$ cm ans $x = 0$, at 1.5 Pa and 94 mT (best magnetized conditions). Only the potential structure at $\theta = 0°$ is presented here, because the potential shape is only enlarged when increasing the tilting angle. As pointed out in a precedent work[47], the space potential evolution can be decomposed into 3 terms, $\phi = \bar{\phi} + \phi_t + \tilde{\phi}$ (see Fig.13(a)), a stationary term $\bar{\phi}$, a transient term ϕ_t which tends to 0 as $t \to \infty$, and an oscillatory term $\tilde{\phi}$. This time evolution is the signature of the capacitive behaviour of the biased flux tube exchanging RF displacement current with the bulk plasma. As the RF potential increases, electrons follows the trend due to their hight mobility. Whereas ions inertia causes the slow decay where the RF potential decreases.

For an aligned electrode ($\theta = 0°$), a total perpendicular capacitance of $C_\perp = 334$ pF is found. This gives a transverse sheath capacitance by unit surface of 3.71 pF/cm^{-2} for $n_0 = 10^{16}$ m^{-3}, which is in good agreement with those calculated by Chen[60]. The input parameters for $L_\perp$ is 20 mm, which takes into account the thickness of the antenna (10 mm), plus a ion Larmor radius extension in the direction perpendicular to **B** at the electrode surface ($\rho_{ci} \approx 5$ mm at $T_e = 5$ eV), which coincides to Chodura's[8] magnetic pre-sheath. The parallel scale $L_\parallel$ is 50 mm, which is not the length antenna – wall, but half of the ion mean free path instead ($\nu_{iN} = 88$ kHz in

our conditions). The input diffusion coefficient is acceptable (5×10^{-2} m^2/s) and the mobility coefficient is $\mu_{i\perp} = 0.36$ m^2/Vs, thus the parallel mobility is $\mu_{i\parallel}^{\mathrm{code}} = \mu_{i\perp}(1 + (\omega_{ci}/\nu_{iN})^2) = 268$ m^2/Vs. This can be compared with the theoretical mobility $\mu = e/M\nu_{iN} \approx 272$ m^2/Vs. Therefore, the coefficient provided as input parameters at $\theta = 0°$ are
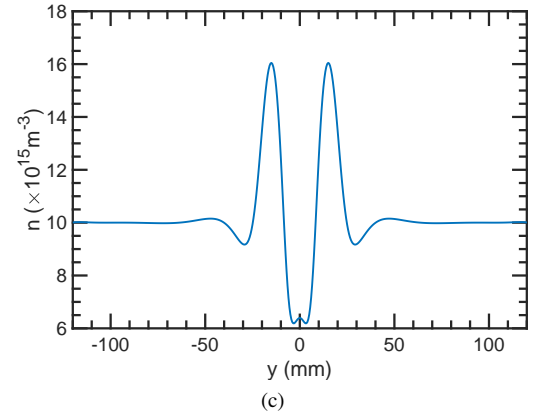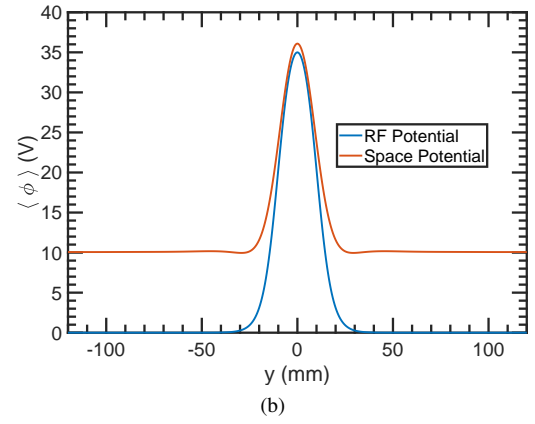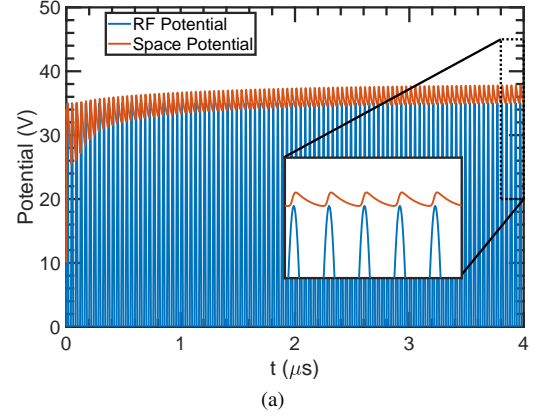

FIG. 13. Code result for the space potential and the density profile in front of the electrode align with magnetic field lines (i.e. $\theta = 0°$). (a) Time evolution of the center of the structure, $\phi(y = 0, t)$, (b) Averaged space potential over the last five periods from Fig.13(a), $\langle\phi\rangle_t(y)$ and (c) Resulting density profile $n(y)$.

acceptable in a physical point of view.

The space potential given by the code is a 2-by-2 dimensional matrix for space and time. To compute the RF transverse current density (using Eq.(19)), the spacial potential structure is averaged over the last five RF periods of the simulation. This potential profile, figure 13(b) is in good agreement with those obtained experimentally at 15 cm from the electrode (see figure 5(h)). Then, the density profile can be calculated in turn by solving equation (20) numerically. The result is plotted in figure 13(c). This typical "bunny ears" shape is recovered in the measurements and is due to transverse currents densities driven by the RF potential structure (ions are accelerated at the edge of the tube due to the transverse **E** field), bringing density on the outer edge of the flux tube, and pumping out the inside of the flux tube.

Finally, figure 14(a) and 14(b) compares the density profiles obtained numerically with those obtained by the experiment. Note that for $\theta = 5°$ and $25°$, the negative y portion of the electrode is much closer to the measuring point than the positive *y* portion: this geometrical aspect coupled with transverse diffusion over a longer path is the consequence of the measured asymmetry of the density profiles at those angles (i.e. $n(y < 0) > n(y > 0)$). Since our model does not take into account any longitudinal dynamics, the computed density profile is perfectly symmetric. Therefore, the higher "ear" is used as reference for the fitting of the curves

The input coefficients at $0°$ are discussed above. But as the angle is increased, the coefficients used are diverging from the physical ones. On the one hand, diffusion is globally unchanged and stays in a range between 0.05 to 0.1 m^2/s, with a maximum at $45°$. On the other hand, the mobility increases up to $\sim 10 \times \mu_{i\parallel}^{\text{theo}}$ at $45°$ and decreases back to a smaller value of $\sim 5 \times \mu_{i\parallel}^{\text{theo}}$ at $90°$. However, the ratio $\mu_{i\perp}/D_{i\perp}$ increases linearly from 0 to $90°$. This growth has a physical meaning though: for small angles, the lateral surface of the flux tube (which communicates with the bulk plasma) is smaller, therefore transverse currents are also smaller. However, for grazing angles (0 and 5 degrees), the input coefficients are correct in a physical point of view, and these inclinations matter the most for the fusion community.

The "bunny ears" have a higher amplitude at small angles. Indeed, the perpendicular currents are mostly driven by density and potential gradients, and those gradients are more important in a narrow flux tube configuration. Just in front of the electrode, there is a density depletion with respect to the bulk plasma. Whereas, on the edge of the flux tube, the potential gradient leads to a density oversupply, generating these "bunny ears shaped curves". Along with this observation, the narrower
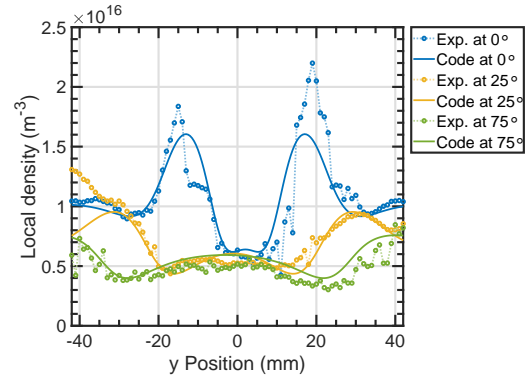
(a)
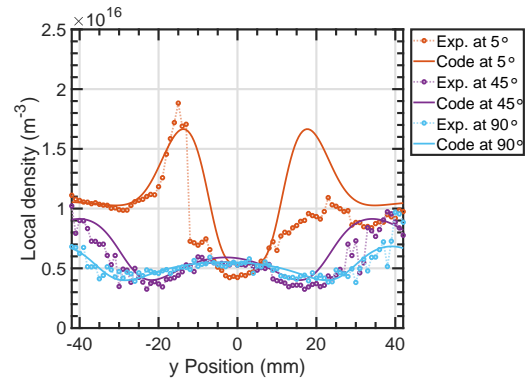
(b)

FIG. 14. Comparison between experiment and code output for the density profiles. The experimental data are taken for 94 mT, 1.5 Pa and 15 cm from antenna at (a) 0, 25 and 75 degrees – (b) 5, 45 and 90 degrees. The gradient length *w* is found to be of the order of 1 cm.

the flux tube, the more it pumps out particles: the density inside the tube is much lower than in the bulk plasma for small angles. Nevertheless, experiment and code are in good agreement, and it seems obvious that the density profile in a plane perpendicular to **B**, in front of an RF antenna, is highly perturbed by transverse currents (which are enhanced by the RF).

V. CONCLUSION

The behaviour of a magnetized plasma in front of a RF electrode (or antenna) is one of major interests for the plasma community. A contribution to this question is provided here, exploiting Langmuir probe measurements inside the linear plasma device ALINE. The probe measurements were performed in several discharge conditions (47 and 94 mT, 1.5 and 3 Pa in He) and 2-D contour plots of the plasma parameters in the front of a tilted antenna with respect to the magnetic field lines were established. The main results from the observation

of these maps are:

- The plasma potential varies strongly in the direction perpendicular to the magnetic field and remains almost constant over several centimetres along the magnetic field at pressure of the order of 2 Pa. The plasma potential is much higher in front of the RF electrode except at low tilting angle (less than $\approx 20°$) for which the plasma biasing due to sheath rectification is very low.

- The density maps exhibit a depleted channel in the central core of the biased flux tube (connected to the antenna). This depletion occurs over few centimetres, the typical scale length of transverse currents. For larger flux tube (i.e. greater tilting angle), the depletion appears only at the inner edge while a density peak grows in the outer edge. In that case the central region is not disturbed.

- The floating potential maps seem to be very dependant on convective electron fluxes and can be negative even inside the biased flux tube.

To understand the plasma potential amplitude in front of the antenna as a function of the tilting angle, a model based on current conservation over different surfaces collecting the current all around the biased flux tube has been developed. At low angle, the active electrode area is almost parallel to the magnetic field so that classical sheath can not operate, and then the self-biasing of the connected plasma is low. At larger angle (over $\approx 20°$) the self-biasing rises up to reach a fraction of the applied RF potential. The experiment and the model are in good agreement, and it was also shown that the plasma potential increases when the magnetic flux tube is wider than the typical transverse scale length of ion currents which deplete the core of the biased channel.

In addition, another model taking into account the computed electron currents received by the probe from the measured density and plasma potential maps (to compute drift current and diamagnetic currents) allows to recover very nicely the measured floating potential, proving that this model is mainly dependant on the electron currents in a plane perpendicular to the magnetic field.

Finally, a numerical fluid model was developed to understand density maps. Using total current density conservation and ion flux conservation inside a homogeneous flux tube connected to the electrode, the code input parameters (such as mobility and diffusion coefficients) are in good agreement with the literature for small tilting angles. The codes outputs allow us to fit the measured density profiles in front of the electrode. Both the numerical result and the experiment display "bunny ears" shaped curves for the density profile. The explanation of this shape is done using transverse ion fluxes (polarization, mobility and diffusion). Inside the flux channel connected to the probe, the density is below the bulk plasma density: the transverse currents deplete the tube, and this depletion is more important for narrow flux tubes. Whereas, on the edge of the tube, there is a density oversupply due to strong potential gradients (i.e. strong $\mathbf{E}$ field). This behaviour is enhanced with the RF and lead to a capacitive behaviour of the RF sheath and of the space potential structure inside the magnetic channel.

This study provides two main contributions regarding the heat fluxes and the triggering of hot spots on RF antennae.

The first is the plasma potential mapping measured in front of a tilted antenna. These maps have shown that the RF plasma potential magnetically connected to the antenna is much lower for small antennae (or grazing tilt angle with respect to magnetic direction), because the connected active area is simply smaller.

The second contribution is the density mapping and especially the density profiles in the direction perpendicular to the magnetic field. They show that the core density, *i.e.* in the central part of the connected flux tube, is strongly depleted compared to the outer plasma when the flux tube width is smaller than 1 or 2 cm (which is the order of magnitude of the ion Larmor radius or the typical RF sheath width if $\omega_{pi} > \omega_{ci}$). However, for larger channel, the density is only depleted over the first radial 1 or 2 centimetres at the inner edge of the magnetic flux tube while the core density is almost undisturbed.

This means that a RF antenna smaller than the typical ion Larmor radius would drain the connected plasma more efficiently. Nevertheless, whatever the (active) size of the antenna, it appears that at the outer edge of the magnetic flux tube there is an overshoot density structure, which can increase the heat flux and may induce hot spots, especially at the edge of the antenna. This has already been observed on antenna structures in Tokamaks.

Finally, concerning the reactive plasma experiments, one can say that the shape of the density profiles reveals that a homogeneous etching on a RF biased substrate cannot be achieved unless its typical width is much larger than a Larmor radius plus a RF sheath width.

The future work will consist in measuring the antenna structure heating with an IR camera to deduce the heat flux and then compare it to the one calculated from our potential and density maps.

DATA AVAILABILITY

All datasets underlying the conclusions of the paper should be available to readers. We encourage authors to deposit their datasets in publicly available repositories (where available and appropriate) or present them in the main manuscript. All research articles must include a data availability statement informing where the data can be found. By data we mean the minimal dataset that would be necessary to interpret, replicate and build upon the findings reported in the article. Dataset can be found at Mendeley Data, DOI : 10.17632/j7rn7tcrr8.1.

Appendix A: Numeric scheme of solving the potential structure

In this section is provided the numerical scheme for the resolution of the potential profile (see section IV A). The partial differential equation (17) needs to be solved numerically. The initial condition of $\varphi(y, t = 0)$ is determined when no perpendicular currents densities are present, i.e. the r.h.s. of Eq.(17) is zero, which gives $\varphi(y,0) = \varphi_{fl}$. Now, equation (17) is discretised in time assuming that $\partial_t \Delta \varphi(y,t) = [\Delta \varphi(y, t+\delta t) - \Delta \varphi(y,t)]/\delta t$, leading to the expression:

$$\Delta_{\perp} \varphi_y^{t+\delta t} = [1 - \beta \nu_{\perp} \delta t] \Delta \varphi_y^t$$
$$+ \frac{\nu_{\perp} \delta t}{\Lambda^2} \left[1 - \frac{e^{\varphi_{fl} - \varphi_y^t}}{2} \left(1 + e^{\varphi_{RF}(y,t)} \right) \right] \quad (A1)$$

where $\nu_{\perp} = \Lambda^2/C_{\perp} \eta \rho_{ci} = D_{i\perp}/\rho_{ci}^2$ is the characteristic frequency of the equation. For time step, $t = 0$, the r.h.s. of this equation is known, and the spatial distribution of φ at time step $t = \delta t$ can be easily found by the mean of finite element method[61]. Let

$$\Delta_{\perp} \varphi_y^{t+\delta t} = \frac{\varphi_{y+\delta y}^{t+\delta t} - 2\varphi_y^{t+\delta t} + \varphi_{y-\delta y}^{t+\delta t}}{\delta y^2}. \quad (A2)$$

Thus, equation (A1) can be rewritten into a simple vectorial form,

$$\bar{\bar{A}} \cdot \overrightarrow{\varphi}^{t+\delta t} = \delta y^2 \, \mathbf{F}(\overrightarrow{\varphi}^t, t, y), \quad (A3)$$

where $\overrightarrow{\varphi}$ is the vector of solutions, $\bar{\bar{A}}$ is a tridiagonal matrix, and $\mathbf{F}$ the r.h.s. of Eq.(A1), depending of the potential structure at previous time step, position, and time. The elements of the matrix are $A_{i,j} = \delta_{i-1,j} - 2\delta_{i,j} + \delta_{i,j-1}$ (here $\delta_{i,j} = 1$ if $i = j$ and else, $\delta_{i,j} = 0$ is the Kronecker symbol). Dirichlet boundary conditions are used, $\varphi_{-\delta y}^{t+\delta t} = \varphi_{(N+1)\delta y}^{t+\delta t} = \varphi_{fl}$. Inverting the matrix gives the potential structure at the next time step, $\varphi(y, t + \delta t)$. This new value of φ is in turn injected in the expression of $\mathbf{F}$ to determine the potential structure at $t + 2\delta t$ by solving Eq.(A3) again, and so on.

Appendix B: Numeric scheme of solving the density structure

The numerical scheme for solving the density profile (see section IV B) is described in the following:

Equation (21) can also be solved numerically by the mean of a finite element difference approach and a matrix inversion. Using the same scheme as in Eq.(A2), the numerical problem rewrites:

$$\bar{\bar{K}} \cdot \overrightarrow{n} = \delta y^2 \, \mathbf{G}(y) \quad (B1)$$

Where $\overrightarrow{n}$ is the density profile solution, $\bar{\bar{K}}$ is a tridiagonal matrix, whose elements are $K_{i,j} = \delta_{i-1,j} - [2 + \delta y^2/\Lambda^2]\delta_{i,j} + \delta_{i,j-1}$, and $\mathbf{G}$ is the r.h.s. of the density equation (21). Again, Dirichlet boundary conditions are used, $n_{-\delta y} = n_{(N+1)\delta y} = n_0$.

[1]R. V. Nieuwenhove and G. V. Oost, Plasma Physics and Controlled Fusion **34**, 525 (1992), DOI : 10.1088/0741-3335/34/4/011.

[2]E. Faudot, L. Colas, S. Heuraux, and J. Gunn, Physics Of Plasmas **17**, 042503 (2010), DOI : 10.1063/1.3357334.

[3]L. Colas, S. Heuraux, S. Bremond, and G. Bosia, Nuclear Fusion **45**, 767 (2005), DOI : 10.1088/0029-5515/45/8/002.

[4]V. A. Godyak and A. A. Kuzovnikov, Fizika Plazmy **1**, 496 (1975).

[5]M. Becoulet, L. Colas, S. Pécoul, J. Gunn, P. Ghendrih, A. Becoulet, and S. Heuraux, Physics Of Plasmas **9**, 2619 (2002), DOI : 10.1063/1.1472501.

[6]J. Takeda, A. Nezu, and H. Akatsuka, IEEE Transactions On Plasma Science **47**, 4250 (2019), DOI : 10.1109/TPS.2019.2928845.

[7]J.-M. Noterdaeme and G. V. Oost, Plasma Physics and Controlled Fusion **35**, 1481 (1993), DOI : 10.1088/0741-3335/35/11/001.

[8]R. Chodura, Physics Of Fluids **25**, 1628 (1982), DOI : 10.1063/1.863955.

[9]E. Faudot, S. Devaux, J. Moritz, S. Heuraux, P. M. Cabrera, and F. Brochard, Review of Scientific Instruments **86**, 063502 (2015), DOI : 10.1063/1.4921905.

[10] J. Allen, R. Boyd, and P. Reynolds, Proceedings of the Physical Society. Section B **70**, 297 (1957), DOI : 10.1088/0031-8949/45/5/013.

[11] J. Allen, Physica Scripta **45**, 497 (1992).

[12] F. Chen, "Lecture notes on langmuir probe diagnostics," Online (2003), Available on F. F. Chen's website : http://www.seas.ucla.edu.

[13] D. Bohm, E. Burhop, and H. Massey, "The characteristics of electrical discharges in magnetic fiels," (McGraw-Hill Book Compagny, inc., New York, 1949) Chap. 2, Avaliable Online : https://archive.org/details/in.ernet.dli.2015.169225.

[14] J. Laframboise, UTIAS Report **100**, 1 (1966), Full text avaliable at : https://apps.dtic.mil/docs/citations/AD0634596.

[15] H. M. Mott-Smith and I. Langmuir, Physical Review **28**, 727 (1926), DOI : 10.1103/PhysRev.28.727.

[16] R. Clements, Journal of Vacuum Science and Technology **15**, 193 (1978), DOI : 10.1116/1.569453.

[17] F. Chen, C. Etievant, and D. Mosher, Physics Of Fluids **11**, 811 (1968), DOI : 10.1063/1.1692002.

[18] T. Dote and H. Amemiya, Journal Of The Physical Society Of Japan **19**, 1915 (1964), DOI : 10.1143/JJAP.3.789.

[19] T. Dote and H. Amemiya, Journal Of The Physical Society Of Japan **22**, 270 (1967), DOI : 10.1143/JPSJ.22.270.

[20] H. Amemiya and T. Dote, Japan Journal Applied Physics **8**, 818 (1969), DOI : 10.1143/JJAP.8.818.

[21] I. Mihaila, M. Solomom, C. Costin, and G. Popa, Contribution Of Plasma Physics **53**, 96 (2013), DOI : 10.1002/ctpp.201310017.

[22] M. Usoltceva, E. Faudot, S. Devaux, S. Heuraux, J. Ledig, G. V. Zadvitskiy, R. Ochoukov, K. Crombe, and J.-M. Noterdaeme, Physics of Plasmas **25**, 063518 (2018), DOI : 10.1063/1.5038666.

[23] M. Usoltceva, E. Faudot, J. Ledig, S. Devaux, S. Heuraux, G. V. Zadvitskiy, R. Ochoukov, J. Moritz, K. Crombe, and J.-M. Noterdaeme, Review of Scientific Instruments **89**, 10J124 (2018), DOI : 10.1063/1.5028267.

[24] F. Chen, Plasma Sources Science and Technology **21**, 055031 (2012), DOI : 10.1088/0963-0252/21/5/055013.

[25] F. Chen, Plasma Sources Science and Technology **18**, 035012 (2009), DOI : 10.1088/0963-0252/18/3/035012.

[26] E. Faudot, J. Ledig, J. Moritz, S. Heuraux, N. Lemoine, and S. Devaux, Physics Of Plasma **26**, 083503 (2019), DOI : 10.1063/1.5096018.

[27] P. Verplancke, R. Chodura, J. Noterdaeme, and M. Weinlich, Contributions To Plasma Physics **36**, 145 (1996), DOI : 10.1002/ctpp.19960360122.

[28] A. Nedospasov and D. Uzdensky, Contributions To Plasma Physics **34**, 478 (1994), DOI : 10.1002/ctpp.2150340259.

[29] A. Aanesland, C. Charles, R. W. Boswell, and M. A. Lieberman, Physics of Plasmas **12**, 103505 (2005), DOI : 10.1063/1.2089227.

[30] E. Kawamura, V. Vahedi, M. A. LiebermaN, and C. K. Birdsall, Plasma Sources Science and Technology **8**, R45 (1999), DOI : 10.1088/0963-0252/8/3/202.

[31] J. G. Laframboise and J. Rubinstein, Physics Of Fluid **19**, 1900 (1976), DOI : 10.1063/1.861425.

[32] J. Ledig, E. Faudot, J. Moritz, S. Heuraux, N. Lemoine, and M. Usoltceva, Plasma Sources Science and Technology **29**, 035007 (2020), DOI : 10.1088/1361-6595/ab56d2.

[33] S.Devaux, E.Faudot, J.Moritz, and S.Heuraux, Nuclear Materials and Energy **12**, 908 (2017), DOI : 10.1016/j.nme.2017.07.003.

[34] I. D. Sudit and F. F. Chen, Plasma Sources Science and Technology **3**, 162 (1994), DOI : 10.1088/0963-0252/3/2/006.

[35] P. A. Chatterton, J. Rees, W. Wu, and K. Al-Assadi, Vacuum **42**, 489 (1991), DOI : 10.1016/0042-207X(91)90022-B.

[36] J. D. Johnson and A. J. T. Holmes, Review of Scientific Instruments **61**, 2628 (1990), DOI : 10.1063/1.1141849.

[37] M. Mausbach, Journal of Vacuum Science And Technology A **15**, 2923 (1997), DOI : 10.1116/1.580886.

[38] C. Steinbrüchel, Journal of Vacuum Science And Technology A **8**, 1663 (1990), DOI : 10.1116/1.576782.

[39] K. Gunther and A. Carlson, Contribution On Plasma Physics **34**, 484 (1994), DOI : 10.1002/ctpp.2150340260.

[40] J. Ledig, E. Faudot, N. Lemoine, S. Heuraux, J. Moritz, and M. Usoltceva, 45th EPS Conference on Plasma Physics , P4.1016 (2018), EPS abstract : http://ocs.ciemat.es/EPS2018PAP/pdf/P4.1016.pdf.

[41] V. Rozhansky, A. Ushakov, and S. Voskoboynikov, Contribution On Plasma Physics **36**, 391 (1996), DOI : 10.1002/ctpp.2150360254.

[42] J. Moritz, E. Faudot, S. Devaux, and S. Heuraux, Physics Of Plasmas **25**, 013534 (2018), DOI : 10.1063/1.5010852.

[43] V. Rozhansky, A. Ushakov, and S. Voskoboynikov, Nuclear Fusion **39**, 613 (1999), DOI : 10.1088/0029-5515/39/5/304.

[44] K. Köhler, J. W. Coburn, D. E. Horne, E. Kay, and J. H. Keller, Journal of Applied Physics **57**, 59 (1985), DOI : 10.1063/1.335396.

[45] A. Metze, D. W. Ernie, and H. J. Oskam, Journal of Applied Physics **60**, 3081 (1986), DOI : 10.1063/1.337764.

[46] A. M. Pointu, Journal of Applied Physics **60**, 4113 (1986), DOI : 10.1063/1.337491.

[47] E. Faudot, S. Heuraux, and L. Colas, Physics Of Plasmas **13**, 042512 (2006), DOI : 10.1063/1.2186530.

[48] R. Bruce, Journal of Applied Physics **52**, 7064 (1981), DOI : 10.1063/1.328703.

[49] J. G. Laframboise and L. W. Parker, Physics Of Fluid **16**, 629 (1973), DOI : 10.1063/1.1694398.

[50] F. F. Chen, J. D. Evans, and D. Arnush, Physics Of Plasmas **9**, 1449 (2002), DOI : 10.1063/1.1462630.

[51] T. K. Popov, M. Dimitrova, P. Ivanova, J. Kovacic, T. Gyergyek, R. Dejarnac, J. Stockel, M. A. Pedrosa, D. Lopez-Bruna, and C. Hidalgo, Plasma Sources Science and Technology **25**, 033001 (2016), DOI : 10.1088/0963-0252/25/3/033001.

[52] I. B. Bernstein and I. N. Rabinowitz, Physics Of Fluids **2**, 112 (1959), DOI : 10.1063/1.1705900.

[53] I. D. Sudit and R. C. Woods, Journal of Applied Physics **76**, 4488 (1994), DOI : 10.1063/1.357280.

[54] A. Savitzky and M. Golay, Analytical Chemistry **8**, 1627 (1964), DOI : 10.1021/ac60214a047.

[55] M. Druyvesteyn, Zeitschrift für Physik **64**, 781 (1930), DOI : 10.1007/BF01773007.

[56] I. G. Brown, A. B. Compher, and W. B. Kunkel, The Physics Of Fluids **14**, 1377 (1971), DOI : 10.1063/1.1693617.

[57] E. Faudot, S. Heuraux, M. Kubic, J. Gunn, and L. Colas, Physics Of Plasmas **20**, 043514 (2013), DOI : 10.1063/1.4802190.

[58] E. Faudot, S. Heuraux, A. Ngadjeu, L. Colas, M. Kubic, and J. P. Gunn, AIP Conference Proceedings **1406**, 125 (2011), DOI : 10.1063/1.3664944.

[59] F. Chen, *Introduction to Plasma Physics and Controlled Fusion*, edited by N. Y. Plenum Publishing Corporation (Plenum, 1984) first Edition, ISBN : 0-306-30755-3.

[60] F. Chen, Plasma Sources Science And Technology **15**, 773 (2006), DOI : 10.1088/0963-0252/15/4/022.

[61] M. Abramowitz and I. Stegun, *Handbook of Mathematical Functions with Formulas, Graphs, and Mathematical Tables* (Dover Publications, 1964) iSBN : 978-0-486-61272-0.